ISSN 1392-1207. MECHANIKA. Vol. 31, No. 4, 2025: 358–367

Failure Analysis of Deep-Drawn Single Piece Pressure Vessels

Ibrahim Savas DALMIS*, Sait Ozmen ERUSLU**
**Tekirdağ Namık Kemal University, Çorlu Faculty of Engineering, Mechanical Engineering Department, 59860, Çorlu-Tekirdağ, Türkiye, E-mail: idalmis@nku.edu.tr*
***Tekirdağ Namık Kemal University, Çorlu Faculty of Engineering, Mechanical Engineering Department, 59860, Çorlu-Tekirdağ, Türkiye, E-mail: oeruslu@nku.edu.tr (Corresponding Author)*

https://doi.org/10.5755/j02.mech.41221

1. Introduction

Pressure vessels play a vital role in modern industry, serving as critical components in the safe storage and transport of fluids under high pressure. As the global demand for energy and industrial processing increases, the structural integrity of pressure vessels becomes more essential than ever. Ensuring the safe operation of these components requires a comprehensive understanding of their design, fabrication, and performance under various loading conditions.

Pressure vessels are crucial equipment in various industries, tasked with storing fluids under high pressures. Due to the inherent risks associated with high pressure, these vessels can pose significant safety hazards [1].

Pressure vessels operate under specific pressure and temperature conditions, handling hazardous substances that pose risks [2].

To ensure adherence to safety standards, various design codes have been developed. The most commonly employed standards are the ASME Boiler and Pressure Vessel Code and the European standard EN 13445 [3].

Pressure vessel failures can be categorized based on considerations related to materials, design, fabrication, and service in accordance with pressure vessel standards, and they can also be categorized based on their dimensions, with distinctions made between thick-shell and thin-shell configurations. [4] Thin-walled pressure vessels are structures characterized by a relatively small ratio of wall thickness to the vessel's radius commonly employed for the storage and transportation of gases and liquids in various industrial applications.

Deep drawing serves as a valuable metal forming technique applicable to the manufacturing of pressure vessels, especially those characterized by cylindrical or cup-shaped configurations. A fire extinguisher features a pressure vessel in a handheld cylindrical form, designed to contain and dispense an extinguishing agent for the purpose of suppressing and putting out fires. Water and powder-based fire extinguishers, are manufactured from mild steel using the deep drawing process.

The deep drawing method allows for the efficient production of seamless and structurally sound pressure vessels, which are essential components of fire extinguishers.

Two types of extinguishers are produced in applications where, in the first type, the cylinder body undergoes deep drawing, and the base and the dome of the extinguisher are shaped independently and later welded onto the cylinder body. In the second type, the entire cylinder section and dome are produced from sheet metal through the deep drawing process.

To achieve a uniform wall thickness and greater height in the deep drawing of pressure vessel process, multiple drawing and ironing stages are employed [5].

Controlling thinning is crucial in pressure vessel deep drawing to ensure the final product meets specified dimensional and structural requirements. Excessive thinning can lead to issues such as reduced strength and integrity of the tube. Engineers and manufacturers often use techniques like finite element analysis to optimize the deep drawing process, aiming to achieve the desired geometry while minimizing thinning and potential defects [6].

Non-destructive testing (NDT) is commonly employed to assess thinning in pressure vessels both during production and throughout their operational lifespan [7].

The characteristics of the material used in deep drawing applications are crucial, particularly its ductility and its ability to handle higher deep drawing ratios effectively. Tensile tests are conducted in three rolling directions to evaluate the material's properties, as these materials must handle multiaxial forces during deep drawing processes. The deep drawing ability of steels is assessed through various forming tests, such as the Nakazima test, Incremental Sheet Forming tests, and Single Point Incremental Forming tests [8].

DC04 is a popular deep drawing steel commonly used in the production of thin-walled pressure vessels. Many studies in the literature focus on the forming ability of DC04. Isik and co-authors investigated the forming ability of DC04 steel sheets during punching [9]. Trzepiecinski and co-authors studied the forming and friction performance of DC04 through bending under tension tests [10]. Efe studied the micro- and macro-scale deformation behavior of DC04 sheet steels under uniaxial tension and biaxial stretching, focusing on cold rolling process strain localization effects using Electron Backscatter Diffraction (EBSD) and digital image processing [11].

The parameters of the deep drawing process are pivotal in attaining the desired level of forming quality. The potential risks of wrinkles and cracks are assessed through the utilization of forming limit diagrams [12].

The elliptical dome shapes adds complexity to the deep drawing process, as it requires careful control of various parameters such as material thickness, lubrication, forming forces, drawing beads, corner radius of dies, etc

The principal residual stresses occurring in a curved dome of a pressure vessel are influenced by a range of factors related to the fabrication and welding processes. During the deep drawing of pressure vessels, the anticipated principal residual stresses are expected to occur at a point near where the most substantial thinning takes place-specifically, just above the punch radius on the sidewall of the elliptical domes [13].

Residual stresses in pressure vessel components are a concern because they can affect the structural integrity and performance of the vessel. They may lead to issues such as stress corrosion cracking, reduced fatigue resistance, and dimensional distortions. The presence of residual stresses in curved structures of pressure vessels like elliptical dome can contribute to thinning over time. Residual stresses can arise during the fabrication and welding processes of pressure vessels. The curved or geometrically complex sections, such as nozzles, shells, or other components, may experience uneven heating and cooling during welding, leading to the development of residual stresses.

The major principal residual stresses typically result from the thermal gradients and plastic deformations. It's important to note that accurately predicting these residual stresses can be a complex task and may require finite element analysis (FEA) or other advanced simulation techniques.

Finite element analysis is utilized to determine the root cause of failure in the analysis of pressure vessels in many studies [14], [15]. Barsoum and co-authors analyzed the root cause failure of a pressure vessel under an internal blast load using finite element analysis. They used the Johnson-Cook failure model to determine the failure zone, considering the effects of plastic strain, strain rate, and temperature [16].

Ghennai and co-authors are focused on studying the effects of plastic anisotropy and hardening behavior in DC04 steel during the deep drawing process using Finite Element Analysis (FEA) [17].

Noraphaiphipaksa and co-authors investigated the stress intensity and failure effects of sight ports on pressure vessels using hydrostatic tests and finite element analysis [14].

Ali Khalfallah studied the mechanical characterization of low carbon steel welded tubes, considering strain hardening through finite element analysis and experimental study [18].

Welding thin plate structures is inherently more challenging than welding thicker plate structures, thin plates are highly sensitive to heat input during the welding process. Throughout the welding process, numerous non-uniform heat inputs contribute to the generation of residual stress distribution. This commonly gives rise to the issue of tensile residual stresses in welding engineering applications [19].

The tensile residual stresses are also very active in causing failure at the notches of cold-worked steels [20].

Simon and co-authors investigated the residual stresses during the deep drawing of a stainless-steel cup. They assessed the balancing characteristics of tensile and compressive residual stresses at the site of the deep-drawn cup using Finite Element Analysis (FEM) [21].

Puoza and co-authors evaluated the residual stresses using the strain gauge indentation method in longitudinally welded electric water heater tanks [22].

Various components and welded sections, such as heads, flanges, and nozzles, are commonly found in pressure vessels. Among these, the welded T-joint is frequently used in their construction. Kollar and co-authors evaluated residual stresses in T-welded sections using the contour method with implemented inverse linear elastic finite element analysis [23]. Wu and co-authors investigated the distribution of residual stresses at the sites of the T-joint by employing both the finite element method and the indentation test method [24].

Peric et al. are focusing on residual stresses in T-welded joints using the sub-modelling technique [25].

The application of a fracture mechanics approach to weld cracks enables a more comprehensive understanding of the structural integrity of welded components, facilitating informed decisions in the areas of design, maintenance, and safety. Aniskovich and his colleagues and investigated operational defects in thin-walled pressure vessel welded joints and main materials using a fracture mechanics approach along with optical studies [26]. Semi-elliptical and elliptical crack contours are used in their study to understand the fracture analysis of thin-walled pressure vessels.

Xio and co-authors are investigating inertia and internal pressure-induced defects in pressure vessels through fracture mechanics-based failure probability analysis [27].

Wang and his colleagues focused on Cweld fracture in thin-walled pressure vessel welds related to stress corrosion cracking. They utilized both finite element analysis (FEA) for stress analysis near the weld crack and microstructural studies [28]. The double ellipsoid heat source model has been implemented into the heat transfer model, coupled with the structural field model for determining the weld heat effect in their analysis.

Balac and co-authors studied maximum strains in the thin-walled pressure vessel weld zone near the nozzles using digital image correlation. They then focused on crack propagation at this stress intensity zone through XFEM analysis [29].

Oh et al. investigated crack growth at stress intensity locations in J-groove welded components, specifically at the reactor pressure vessel closure head and nozzles [30].

The present study investigates the failure behavior of a fully deep-drawn, fire extinguisher-type pressure vessel. Unlike previous works that primarily examined partially deep-drawn designs with welded components, this research emphasizes the combined influence of high draw ratios and welding on structural failure. To this end, tensile and hydrostatic strength tests are conducted alongside detailed finite element analyses.

The FEA is structured in two stages. In the first, residual stresses induced by weld heat input are assessed to understand their contribution to localized weakening and crack initiation. In the second stage, stress intensity at critical crack tips is evaluated to pinpoint the conditions leading to fracture. This comprehensive approach aims to clarify the role of weld-affected zones in catastrophic failure, particularly in the curved sections of the vessel.

2. Material and Methods

2.1. Fire extinguisher type pressure vessel characteristics

The material used in the production of the fire extinguisher-type pressure vessel is DC-04 (DIN EN-10130), known for its ductility and suitability for higher deep drawing ratios.

The chemical composition of the material is provided in Table 1 [31].

The pressure vessel for the portable fire extinguisher is produced using a two-stage deep-drawing process, with maximum drawing ratios of 2 and 1.3 for the first and second stages according to EN 3-8:2021 standards. The reduction ratios are 50% and 23%, respectively, with a starting blank diameter of 400 mm. These deep drawing parameters are provided by the manufacturer.

The thickness of the sheet steel at the start of the drawing is 1.5 mm. The variation in thickness of the pressure vessel at the end of the deep-drawing process is shown in Fig. 1.

Table 1

Chemical Composition of DC04 Low Carbon Steel

Standard Number	EN 10130
Producer Number	Erdemir-7114
C	0.08
P	0.03
S	0.03
Mn	0.04
Ti	0.065

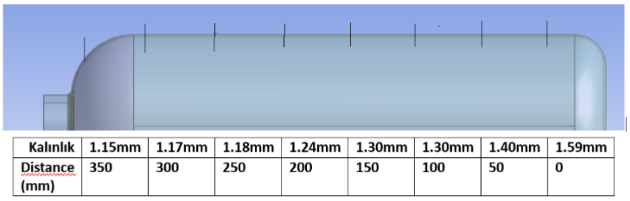

Kalınlık	1.15mm	1.17mm	1.18mm	1.24mm	1.30mm	1.30mm	1.40mm	1.59mm
Distance (mm)	350	300	250	200	150	100	50	0

Fig. 1 Thickness variation of the fire extinguisher

The MAG welding operation used to apply the bush on the head section and the base section was conducted in previous research [32], by the TS EN ISO 15614-1 standards, as shown Fig. 2 and Table 2.

Here, heat input was calculated according to ISO/TR 18491:2015 standard [33]

$$H = \frac{\eta\ V\ A\ 60}{s}\ , \tag{1}$$

where H is heat input (J/mm), η is an arc weld efficiency, V is an arc weld voltage, A is an arc weld current, s is the travel speed (mm/min). The mechanical properties of the sheet material are provided in Table 3. It is observed that both yield strength and tensile strength increase, while ductility decreases with higher cold reductions after two stages.

The strain hardening coefficient and hardening coefficient at the Table 3 are calculated according to the Holloman equation by using true stress strain curve given below [34].

$$\sigma_T = K\varepsilon^n\ . \tag{2}$$

Here K is the strength coefficient, n is the strain hardening coefficient.

These values in Table 3 are obtained for the log true stress-strain curve using linear regression with the least squares method.

2.2. Hydrostatic test

The hydrostatic test is performed to ensure that the vessel can safely contain the intended working pressure without failing, and also to assess factors such as burst pressure and the failure zone, as shown in the figure below. Standards for Portable Fire Extinguishers

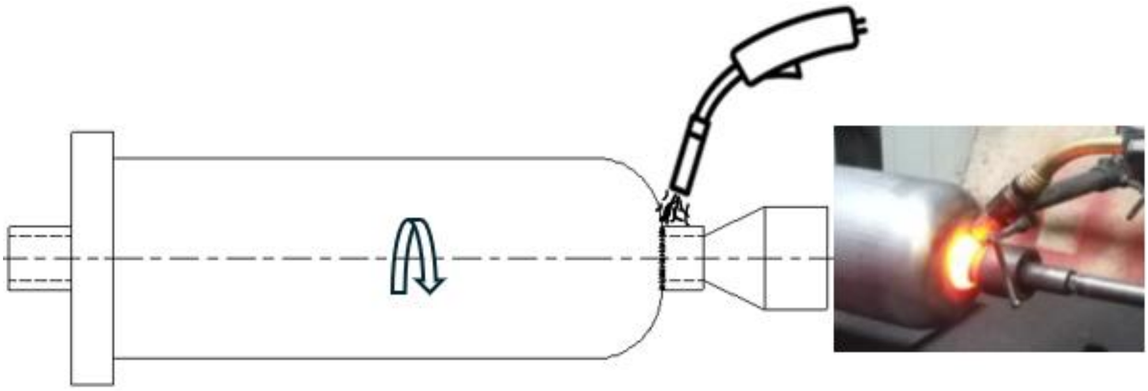

a

b

Fig. 2 MAG welding operations setup graphic applied to deep-drawn fire extinguisher (a) and view of MAG welding operation (b)

Table 2

MAG weld parameters at welding of pressure vessel

Specimen	Welding current, A	Welding voltage, V	Welding speed, mm/min	Torch distance, mm	Weld efficiency, η	Total power, W
1	100	14	300	2	0.7	980
2	100	14	200	2	0.7	980
3	125	15	300	2	0.7	1312
4	125	15	200	2	0.7	1312
5	140	15.6	300	2	0.7	1534
6	140	15.6	200	2	0.7	1534

Table 3

The mechanical properties of welded and non-welded samples

Operation	Yield Strength, MPa	Tensile Strength, MPa	Elongation, %	Strength Coefficient, K, MPa	Hardening Coefficient, n	Anisotropy ratio, $r90$
Cold Worked	210	350	38	575	0.18	1.6
Cold Worked + Deep Drawn	597	642	6	2749	0.48	1.6

TS EN 3-8 covers the construction, resistance to pressure, and mechanical tests for extinguishers with a maximum allowable pressure equal to or lower than 30 bar. According to these standards the burst pressure should not be less than 2.7 times the permissible pressure, and a 81 bar test pressure is applied during tests. This process also allows for the identification of the maximum pressure the tube can withstand and provides insights into the failure zone, which refers to the conditions or pressure range at which the tube fails. All pressure vessels do not fail at test pressure. The burst pressure of the tested vessels was found to be approximately 120 bar. The hydrostatic test setup graphic and typical images of the test samples' failure zones used in the experiments are given in Fig. 3.

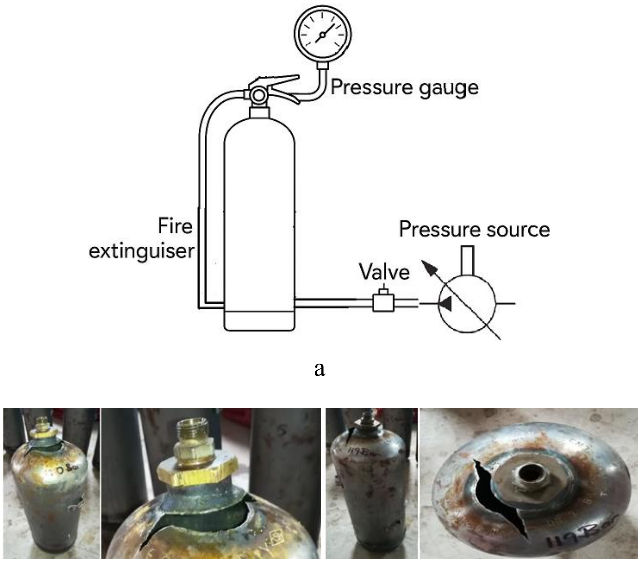

a

b

Fig. 3 Hydrostatic test setup graphic (a) and Failure zones at the burst pressure vessels (b)

3. Result and Discussion

3.1. Microhardness measurements

After grinding and polishing, the hardness samples were etched. HV1 Vickers microhardness measurements were then taken at five different points, including the weld fusion zone, the heat-affected zone (HAZ), and the base metal zone, using the Microbul-1000-DN microhardness tester (Fig. 4).

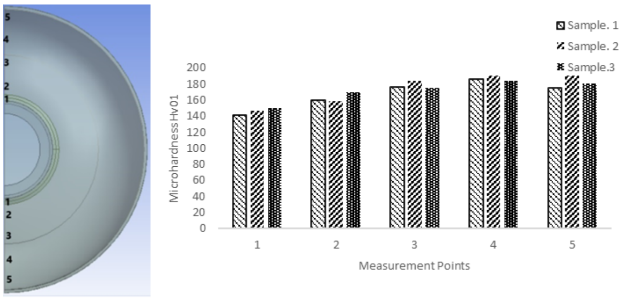

Fig. 4 Microhardness measurements at the head of the pressure vessel

It can be seen from the figure that the hardness decreases in both the weld fusion zone and the weld-affected zone, which is the main reason for the reduced strength weld affect at thinnest section after deep drawing.

3.2. Microstructure investigation

In this section, a microstructural investigation is conducted on the deep-drawn tube shell and head section, with a specific focus on the curved head section, and weld-affected zone. The ferritic and perlitic microstructure of DC04 before deep drawing is given at the figure below (Fig. 5).

In the shell section, after deep drawing, longitudinally oriented, highly elongated ferrite grains can be observed in the figure below. In the elongation and transverse direction, no cracks are observed. (Fig. 6).

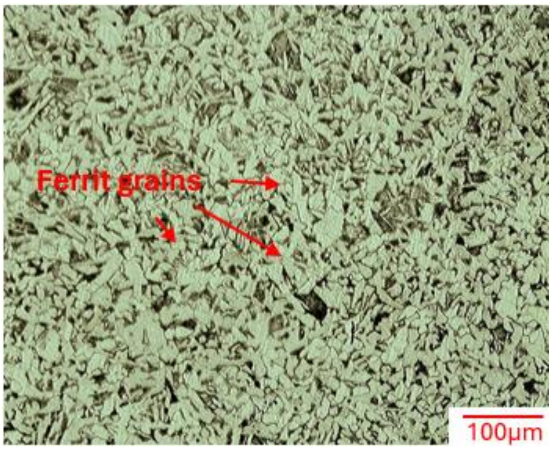

Fig. 5 Microstructure of DC04 before deep drawing

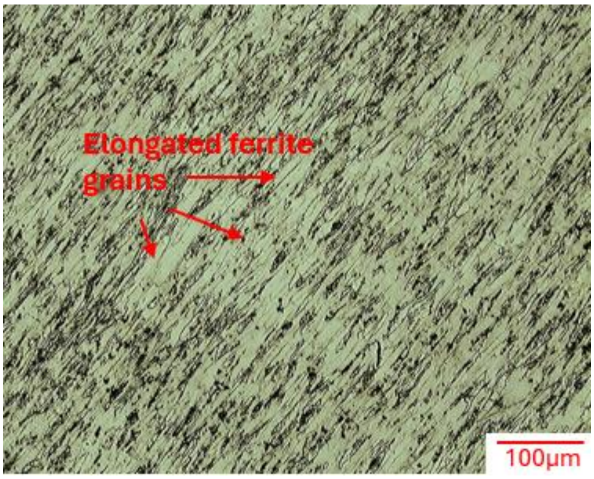

Fig. 6 The oriented ferrite grains at shell section

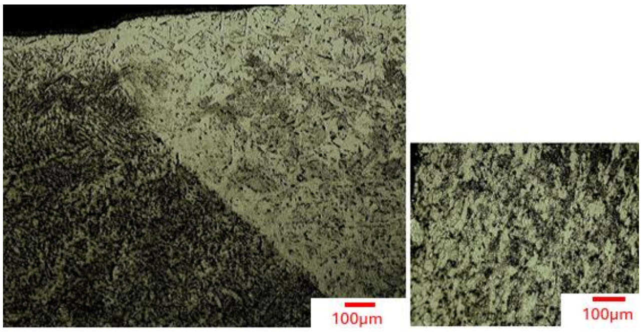

Fig. 7 Weld heat affected zone recrystallized grains

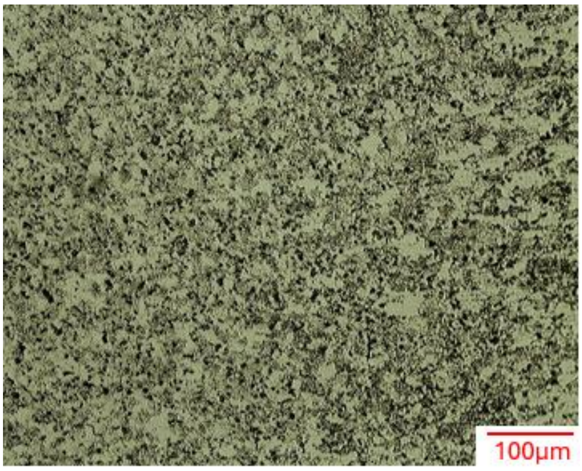

Fig. 8 Weld heat affected zone boundaries with recrystallized grains

The weld and heat-affected zone at the curved head section are shown in the Fig. 7 and Fig. 8. No weld defects were observed in the weld fusion zone. The figures indicate that weld fusion is effective in the HAZ zone at the transition and also at the far boundaries of HAZ zone, where oriented grains transform into recrystallized grains.

The grain orientation at the curved thinned head section is shown in the following Fig. 9. It can be observed that the ferritic grain orientation is present, and the grain sizes have decreased compared to the shell section.

The microhardness and microstructural studies indicate a decrease in the strength of the HAZ zone, where recrystallization has occurred in the elongated grains.

3.3. Finite element analysis

The couple-field thermomechanical finite element analysis is performed to better understand the effects of residual stresses and thermal conditions on the failure zone. In the first stage, a thermal analysis is conducted on the weld heat-affected zone at the head section, based on the heat source parameters. In the second stage, the temperature changes from the thermal analysis are used as thermal load inputs for the subsequent mechanical analysis. The pressure vessel model and thermal and mechanical boundary conditions used in the finite element analysis are illustrated in Fig. 10, with symmetry boundary conditions applied to reduce computational effort.

The Gauss heat flux technique was incorporated into the finite element model for thermal analysis to simulate the weld arc, involving the customization of Gauss heat flux parameters as described in the following section.

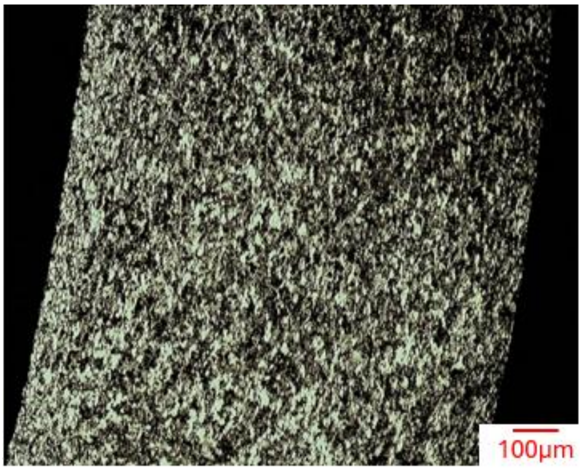

Fig. 9 The oriented ferrite grains at curved head section

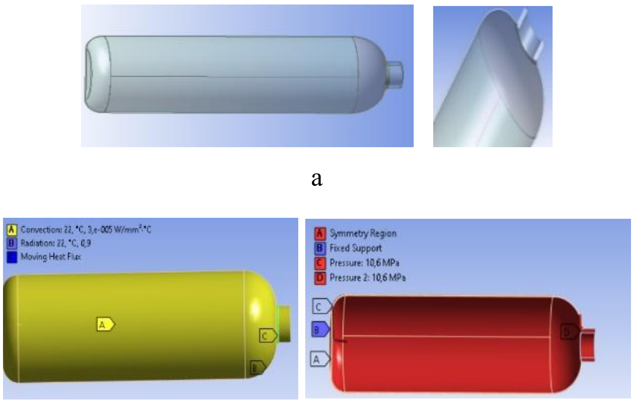

a

b

c

Fig. 10 Pressure vessel model (a), thermal boundary conditions (b) and mechanical boundary conditions (c)

The Gauss heat source density of the weld was characterized by the following formula based on the heat source radius [35, 36]:

$$q_0 = \frac{3}{\pi R^2} Q , \tag{3}$$

$$Q = \eta U I , \tag{4}$$

where q_0 is heat source density per heat effected area, Q is total heat input, η is an arc weld efficiency, U is an arc weld voltage, I is an arc weld current, r is the surface flux at radius, R is weld pool radius.

The Gauss heat distribution parameters in the moving heat line model for finite element analysis were derived from experimental weld parameters presented in Table 2, utilizing the heat input formula specified in Table 4.

Table 4

The moving heat source parameters at the numerical study

Weld Speed	13.33 mm/s
Weld Current Heat Radius R	2.8 mm
Weld Power Density q	49.1 W/m^2
Weld Time t	6.26 s

Quadratic ten-node tetrahedral thermal and structural solid elements (Solid291 and (Solid187) are used in the finite element models to optimize meshing transition at the curved and cylindrical sections and to improve sensitivity by increasing the number of numerical integration points. The mesh element size is determined to be 5 mm at the head section and refinement is applied at weld heat applied face, considering element quality for effective heat flux and temperature variation optimal for computational effort in the couple field analysis, as illustrated in Fig. 11.

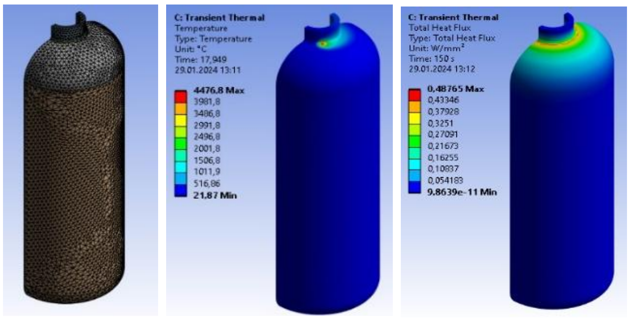

a b c

Fig. 11 The finite element model mesh (a), temperature variation (b) and heat flux variation at the weld heat affected zone (c)

Temperature-dependent specific heat and conductivity values for the DC04 material were obtained from the literature [37, 38]

Thermal boundary conditions, including the convection coefficient value and radiation rate, were defined as 30 W/m^2 and 0.9, respectively [39].

After thermally induced residual stresses are determined, the second stage of the analysis implements these residual stresses. Internal pressure is then applied to complete the failure analysis. During the nonlinear failure analysis, the mechanical properties of the pressure vessel, including the effects of deep drawing, are used.

A nonlinear static analysis is conducted using the bilinear isotropic hardening material model at the second stage. The study evaluates plasticity in the failure zone and Von Mises stresses, which are then compared with experimental results. The residual stress state in the weld heat-affected zone (HAZ) is indeed crucial for the failure analysis of pressure vessels. Weld heat-affected residual stresses evaluated by FEM analysis are given at the following Fig. 12.

The residual stress results indicate that tensile residual stresses are effective at the weld heat affected zone which is known that tensile residual stresses may contribute to the initiation and propagation of cracks. At the second step, the internal pressure is determined based on the burst pressure values obtained from hydrostatic tests. The results of the failure analysis at the end of the second step are provided in Fig. 13 and Fig. 14.

The figures illustrate that maximum stresses and strains occur at the shell sections, while minimum stresses are observed at the head zone of the pressure vessel. These observations are consistent with analytical stress results provided for circumferential and axial stresses in thin-walled pressure vessels subjected to internal pressure [28]. Fig. 14 shows that the plastic strains and yield stresses in the weld heat-affected zone influence the pressure vessel's strength.

While it is recognized that high stresses occur at the shell sections of a pressure vessel, it is noteworthy that the shape of the stress curve at the dome section and the stress concentrations introduced at the transition sections, particularly in welded zones, play a significant role in the failure of pressure vessels [28, 40].

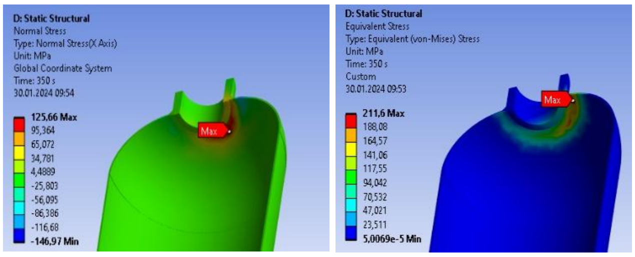

a b

Fig. 12 Tensile residual stresses at weld affected zone (a) and von Mises residual stresses at weld affected zone (b)

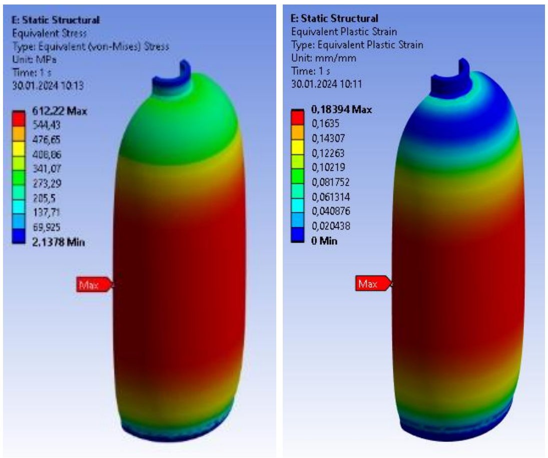

a b

Fig. 13 The von Mises stress (a) and plastic strain (b) results of pressure vessel shell sections for 10.6 MPa internal pressure

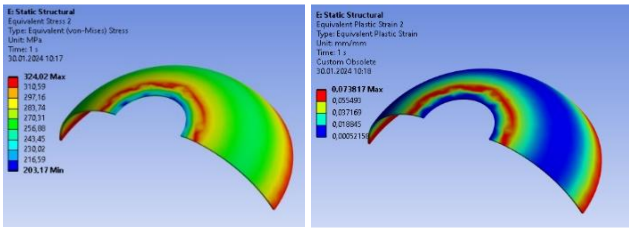

a b

Fig. 14 The von Mises stress (a) and plastic strain (b) results of pressure vessel welded cap sections for 10.6 MPa internal pressure

The crack opening mode is also studied with a semi-elliptical crack at failure zones to understand the crack opening failure mechanism. Semi elliptical crack zones are determined from the failure zones observed in hydrostatic burst pressure tests. The singularity is reduced by positioning the mid-side nodes at the quarter points in the hex-dominant mesh around the crack front, which should be quadratic.

It is seen from the figures that the Mode I dominated crack opening is observed at crack zones, which is in good agreement with experimental hydrostatic tests (Fig. 15 and Fig. 16). The numerical results are compared with the

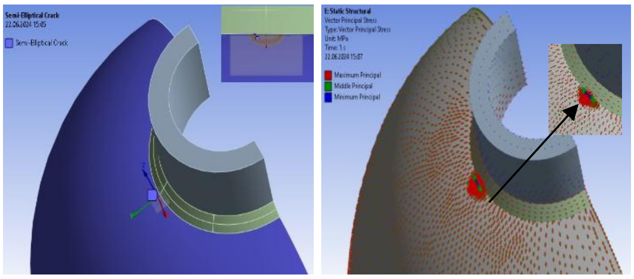

a b

Fig. 15 Semi-elliptical crack at head section (a) and opening mode in semi-elliptical crack at the head section weld (b)

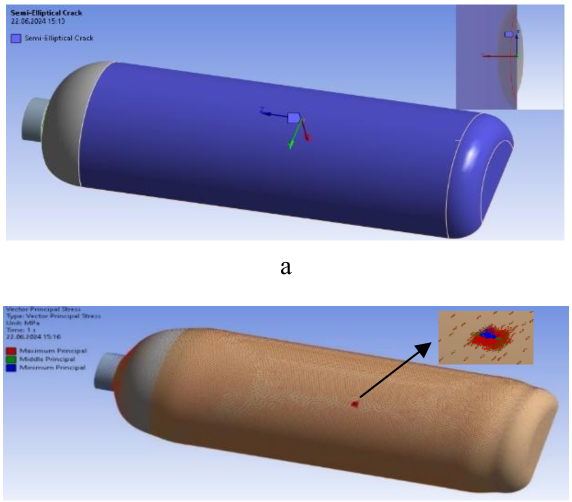

a

b

Fig. 16 Semi-elliptical crack at shell section (a) and crack opening mode in semi-elliptical crack at shell section (b)

analytical results obtained from the stress intensity factor calculation derived by Irwin for semicircular crack from the equation below for critical pressure [41]

$$K_I = \frac{\sigma\sqrt{\pi a}}{E(k)}\left(Sin^2\theta + \frac{a^2}{c^2}Cos^2\theta\right)^{\frac{1}{4}}, \tag{5}$$

$$E(k) = \left[1 + 1.47\left(\frac{a}{c}\right)^{1.64}\right]^{\frac{1}{2}}, \tag{6}$$

where a is the crack depth, c is the half surface length of the semi-elliptical crack.

Here, stress σ at the pressure vessel is defined as follow for shell and curve section respectively:

$$\sigma_\theta = \frac{PR}{t}, \tag{7}$$

$$\sigma_z = \frac{PR}{2t}, \tag{8}$$

where R is the pressure vessel inner radius, σ_θ and σ_Z are hoop and longitudinal stresses respectively.

Critical pressure may be defined by Eqs. (5), (6) and (7) according to the stress intensity factor [42]:

$$P_{cr} = \frac{K_c\, t}{F\, R\sqrt{\pi a}}, \tag{9}$$

$$K_C = K_I, \tag{10}$$

where K_c is fracture toughness determined experimentally, F is the geometric correction factor, t is the pressure vessel thickness. The critical pressure can also be defined according to the yield strength σ_y [42]

$$P_{cr} = \frac{2\sigma_y\, t}{\sqrt{3}\, R}. \tag{11}$$

The critical pressure in Equation 9 is determined from hydrostatic tests. The variation of the critical stress intensity factor for a shell and curved head section of a pressure vessel, with respect to the crack length to thickness ratio, is shown in Fig.| 17.

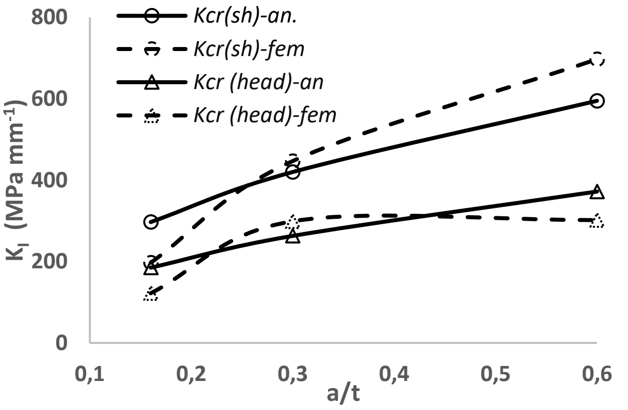

Fig. 17 The critical stress intensity factor at shell and curve section of pressure vessel: P_{cr} = 12 MPa, a / c = 0.5, σ_{cr} = 498 MPa

In Fig. 17, *Kcr(sh)-an*, *Kcr(head)-an* refer to the analytical solutions for the shell and head sections, respectively. Whereas *Kcr(sh)-fem*, *Kcr(head)-fem* refer to the finite element modeling solutions for the shell and head sections, respectively.

The figure indicates that critical stress intensity is achieved at lower values for smaller crack length-to-thickness ratios. Numerical and analytical results demonstrate that the critical fracture stress intensity is lower in the head section of the pressure vessel, where catastrophic failure occurs during hydrostatic tests.

4. Conclusions

This study systematically investigated the failure mechanisms of fully deep-drawn, thin-walled pressure vessels used in fire extinguisher applications, focusing particularly on the influence of weld-induced residual stresses and geometric thinning in curved regions. A comprehensive experimental and numerical approach, including tensile and microhardness testing, hydrostatic burst pressure evaluation, microstructural analysis, and coupled-field thermomechanical finite element simulations, was employed.

The findings clearly indicate that the weld heat-affected zone (HAZ), particularly in the head section of the vessel, serves as a critical location for failure initiation. Microstructural evaluations revealed grain recrystallization and reduced hardness in this region, corresponding with localized thinning. Hydrostatic burst tests confirmed that failure consistently occurred in these weld-affected areas.

Residual stresses were obtained through thermomechanical coupled-field FEM analysis, considering the nonlinear behavior of DC04 steel. The results indicate the presence of tensile residual stresses in the weld heat-affected zone (HAZ), which are known to be a dominant factor contributing to failure. Both hydrostatic testing and thermomechanical FEM results reveal that the weld-affected region at the thinnest section of the pressure vessel dome is the critical area during catastrophic failure. Stress intensity effects at the shell and dome sections of the pressure vessel were also analyzed using a semi-elliptical crack model at these critical locations. A Mode I-dominated tensile fracture mechanism was observed in the fracture zones, consistent with the burst patterns seen in experimental tests.

Overall, the study highlights the significant impact of welding-induced thermal gradients and geometrical features on the structural performance of fully deep-drawn vessels. These results underscore the importance of precise process control in welding and forming operations and advocate for the continued use of integrated experimental and computational methods in predicting and preventing catastrophic failures in pressure vessels.

Future work may include parametric optimization of welding parameters and post-weld heat treatment strategies to reduce residual stresses and enhance structural performance and service life.

References

1. **Bassani, P. V.; Amorim, H. J.; Iturrioz, I.** 2009. Pressure Vessel Failure Analysis, 20th International Congress of Mechanical Engineering, Proceedings of COBEM 2009.
2. **Jegatheesan, J.; Zakaria, Z.** 2018. STRESS ANALYSIS ON PRESSURE VESSEL, Environment & Ecosystem Science (EES) 2(2): 53-57. https://doi.org/10.26480/ees.02.2018.53.57.
3. 2021 ASME Boiler & Pressure Vessel Code VIII Rules For Construction of Pressure Vessels, Division 3 2021. Edt. The American Society of Mechanical Engineers New York, USA.
4. **Dwivedi, N.; Kumar, V.** 2012. Burst Pressure Prediction of Pressure Vessel using FEA, International Journal of Engineering Research & Technology (IJERT) 1(7): 1-6.
5. **Sedighi, M.; Rasti, M.** 2008. An investigation on manufacturing process parameters of CNG pressure vessels, The International Journal of Advanced Manufacturing Technology 38: 958-964. https://doi.org/10.1007/s00170-007-1139-0.
6. **Zaid, A. I. O.** 2016. Deep drawing mechanism, parameters, defects and recent results: state of the art, IOP Conference Series: Materials Science and Engineering 146: 012009. https://doi.org/10.1088/1757-899X/146/1/012009.
7. **Vukelic, G.; Vizentin, G.; Bozic, Z.; Rukavina, L.** 2021. Failure analysis of a ruptured compressor pressure vessel, Procedia Structural Integrity 31: 28–32. https://doi.org/10.1016/j.prostr.2021.03.006.
8. **Gandla, P. K.; Pandre, S.; Suresh, K.; Kotkunde, N.; Singh, S. K.** 2023. Evaluation of fracture limits of deep drawing quality steel using stretching incremental forming and double-notched tensile tests, Journal of the Brazilian Society of Mechanical Sciences and Engineering 45: 148. https://doi.org/10.1007/s40430-023-04066-4.
9. **Isik K.; Gerstein G.; Gutknechta F.; Clausmeyera T.; Nürnbergerb F.; Maier H.J.; Tekkaya A.E.** 2016. Investigations of ductile damage in DP600 and DC04 deep drawing, Procedia Structural Integrity 2: 673-680. https://doi.org/10.1016/j.prostr.2016.06.087.
10. **Trzepiecinski, T.; Lemu, H. G.** 2020. Efect of Lubrication on Friction in Bending under Tension Test-Experimental and Numerical Approach, Metals 10(4): 544. https://doi.org/10.3390/met10040544.
11. **Efe M.** 2019. Strain Localization Behavior of Cold-Rolled Deep-Drawing Steels, Celal Bayar University Journal of Science 15(1): 81-86. https://doi.org/10.18466/cbayarfbe.471039.
12. **Wang, H.; Zhou, J.; Luo, Y.; Tang, P.; Chen, Y.** 2014. Forming of Ellipse Heads of Large-scale Austenitic Stainless Steel Pressure Vessel, Procedia Engineering 81: 837-842. https://doi.org/10.1016/j.proeng.2014.10.085.
13. **Colgan, M.; Monaghan, J.** 2003. Deep drawing process: analysis and experiment, Journal of Materials Processing Technology 132(1-3): 35-41. https://doi.org/10.1016/S0924-0136(02)00253-4.
14. **Noraphaiphipaksa, N.; Poapongsakorn, P.; Hasap, A.; Kanchanomai, C.** 2020. Failure analysis of pressure vessel with sight ports using finite element analysis, Engineering Failure Analysis 117: 104791. https://doi.org/10.1016/j.engfailanal.2020.104791.
15. **Hazizi, E.; Ghaleeh, M.** 2023. Design and Analysis of a Typical Vertical Pressure Vessel using ASME Code and FEA Technique, Designs 7(3): 78. https://doi.org/10.3390/designs7030078.
16. **Barsoum, I.; Lawal, S. A.; Simmons, R. J.; Rodrigues, C. C.** 2018. Failure analysis of a pressure vessel subjected to an internal blast load, Engineering Failure Analysis 91: 354-369. https://doi.org/10.1016/j.engfailanal.2018.04.037.
17. **Ghennai, W.; Boussaid, O.; Bendjama, H.; Haddag, B.; Nouari, M.** 2019. Experimental and numerical study of DC04 sheet metal behaviour-plastic anisotropy identification and application to deep drawing, The International Journal of Advanced Manufacturing Technology 100: 361-371. https://doi.org/10.1007/s00170-018-2700-8.
18. **Khalfallah, A.** 2014. Experimental and numerical assessment of mechanical properties of welded tubes for hydroforming, Materials and Design 56: 782-790. https://doi.org/10.1016/j.matdes.2013.11.051.
19. **Coules, H. E.** 2013. Contemporary approaches to reducing weld induced residual stress, Materials Science and Technology 29(1): 4-18. https://doi.org/10.1179/1743284712Y.0000000106.
20. **Lingyan, Z.; Yinghao, C.; Fuqiang, Y.** 2018. Effect of Cold Working on the Residual Stress around the Notch

front of Stress Corrosion Cracking, IOP Conference Series: Materials Science and Engineering 408: 012007. https://doi.org/10.1088/1757-899X/408/1/012007.

21. **Simon, N.; Erdle, H.; Walzer, S.; Gibmeier, J.; Böhlke, T.; Liewald, M.** 2021. Residual stresses in deep-drawn cups made of duplex stainless steel X2CrNiN23-4, Forschung im Ingenieurwesen 85: 795-806. https://doi.org/10.1007/s10010-021-00497-4.
22. **Puoza, J. C.; Hua, X.; Moro, A.; Akayeti, A.; Baidoo, P.** 2017. Assessment of Mechanical Properties Residual Stresses and Diffusible Hydrogen of Longitudinal Weld in Electric Water Heater Tanks, Journal of Manufacturing and Materials Processing 1(2): 19. https://doi.org/10.3390/jmmp1020019.
23. **Kollár, D.; Völgyi, I.; Joó, A. L.** 2023. Assessment of residual stresses in welded T-joints using contour method, Thin-Walled Structures 190: 110966. https://doi.org/10.1016/j.tws.2023.110966.
24. **Wu, G.; Luo, J.; Li, L.; Long, Y.; Zhang, S.; Wang, Y.; Zhang, Y.; Xie, S.** 2022. Control of Welding Residual Stress in Large Storage Tank by Finite Element Method, Metals 12(9): 1502. https://doi.org/10.3390/met12091502.
25. **Perić, M.; Tonković, Z.; Maksimović, K. S.; Stamenković, D.** 2019. Numerical Analysis of Residual Stresses in a T-Joint Fillet Weld Using a Submodeling Technique, FME Transactions 47(1): 183-189. https://doi.org/10.5937/fmet1901183P.
26. **Aniskovich, E. V.; Lepihin, A. M.; Moskvichev, V. V.** 2019. Evaluating the Static Cracking Resistance of Thin-Walled Pressure Vessels, Inorganic Materials 55(15): 1503-1510. https://doi.org/10.1134/S0020168519150020.
27. **Xiao, Z.; Shi, J.; Cao, X.; Xu, Y.; Hu, Y.** 2018. Failure probability analysis of pressure vessels that contain defects under the coupling of inertial force and internal pressure, International Journal of Pressure Vessels and Piping 168: 59–65. https://doi.org/10.1016/j.ijpvp.2018.09.005.
28. **Wang, M.; Guo, K.; Wei, Y.; Chen, J.; Cao, C.; Tong, Z.** 2023. Failure analysis of cracking in the thin-walled pressure vessel of electric water heater, Engineering Failure Analysis 143(B): 106913. https://doi.org/10.1016/j.engfailanal.2022.106913.
29. **Balac, M.; Grbovic, A.; Petrovic, A.; Popovic, V.** 2018. Fem analysis of pressure vessel with an investigation of crack growth on cylindrical surface, Maintenance and Reliability 20(3): 378-386. https://doi.org/10.17531/ein.2018.3.5.
30. **Oh, S. H.; Ryu, T. Y.; Park, S. H.; Won, M. G.; Kang S. J.; Lee, K. S.; Lee, S. H.; Kim, M. K.; Choi, J. B.** 2015. Evaluation of J-groove weld residual stress and crack growth rate of PWSCC in reactor pressure vessel closure head, Journal of Mechanical Science and Technology 29(3): 1225-1230. https://doi.org/10.1007/s12206-015-0236-5.
31. Erdemir Product Katalog. Available at: https://www.erdemir.com.tr/storage/uploads/2023/10/1ff62aadb0ec3dc42572e2d090067615.pdf
32. **Gul, H.** 2019. Seyyar Yangın Söndürme Cihazlarının İmalatında Uygulanan İdeal Gaz Altı Alın Kaynak Prosedürü Değerlerinin Tespiti. Master of Science Thesis, Department of Mechanical Engineering, Tekirdağ Namik Kemal University Graduate School of Natural and Applied Sciences, Turkiye.
33. **Rajkumar, V.; Shanmugam, N. S.; Kumar, N. P.; Kumar, K. K.; Kannan, A. R.** 2024. Microstructure, mechanical properties, and corrosion behaviour of wire arc additive manufactured martensitic stainless steel 410 for pressure vessel applications, International Journal of Pressure Vessels and Piping 209: 105171. https://doi.org/10.1016/j.ijpvp.2024.105171.
34. **Afkhami, S.; Amraei, M.; Javaheri, V.; Ghafouri, M.; Björk, T.; Salminen, A.; Zhao, X. L.** 2024. Flow and hardening behavior in the heat-affected zone of welded ultra-high strength steels, Welding in the World 68(5), 1001-1016. https://doi.org/10.1007/s40194-024-01703-x.
35. **Fanous, I. F. Z.; Younan, M. Y. A.; Wifi, A. S.** 2003. 3-D Finite Element Modeling of the Welding Process Using Element Birth and Element Movement Techniques, ASME Journal of Pressure Vessel Technology 125(2): 144-150. https://doi.org/10.1115/1.1564070.
36. **Eruslu, S. O.; Akbulut, I. B.; Dalmis, I. S.** 2024. Effects of Weld Heat Input on Mechanical Characteristics of Low Carbon Sheet Steels, Mechanics 30(2): 188-198. https://doi.org/10.5755/j02.mech.34356.
37. **Wernicke, S.; Thier, U.; Hahn, M.; Tekkaya, E.** 2020. Controlling material flow in incremental sheet-bulk metal Forming by thermal grading, Procedia Manufacturing 50: 257-264. https://doi.org/10.1016/j.promfg.2020.08.048.
38. **Sun, J.; Nitschke-Pagel, T.; Dilger K.** 2021. Influence of temperature- and phase-dependent yield strength on residual stresses in ultra-high strength steel S960 weldments, Journal of Materials Research and Technology 15: 1854-1872. https://doi.org/10.1016/j.jmrt.2021.09.050.
39. **Chen, B. Q.; Hashemzadeh, M.; Soares, C. G.** 2014. Numerical and experimental studies on temperature and distortion patterns in butt-welded plates, The International Journal of Advanced Manufacturing Technology 72: 1121-1131. https://doi.org/10.1007/s00170-014-5740-8.
40. **Wang, M.; Guo, K.; Wei, Y.; Cao, C.; Tong, Z.** 2023. Welding process optimization for the inner tank of the electric water heater by numerical simulation and experimental study, Journal of Manufacturing Processes 85: 52-68. https://doi.org/10.1016/j.jmapro.2022.11.025.
41. **Espinoza, L.; Bea, J. A.; Chakraborty, S.; Galatro, D.** 2023. Comparison of the stress intensity factor for a longitudinal crack in an elliptical base gas pipe using FEM vs. DCT methods, Forces in Mechanics 13: 100233. https://doi.org/10.1016/j.finmec.2023.100233.
42. **Alizadeh, E.; Dehestani, M.** 2018. Analytical and numerical fracture analysis of pressure vessel containing wall crack and reinforcement with CFRP laminates, Thin-Walled Structures 127: 210-220. https://doi.org/10.1016/j.tws.2018.02.009.

I. S. Dalmis, S. O. Eruslu

FAILURE ANALYSIS OF DEEP-DRAWN SINGLE PIECE PRESSURE VESSELS

Summary

This study presents a comprehensive failure analysis of fully deep-drawn, thin-walled pressure vessels used in fire extinguisher applications, focusing on the effects of deep drawing and welding processes. Hydrostatic burst pressure testing, tensile and microhardness measurements, microstructural evaluations, and coupled thermomechanical finite element analysis (FEA) were performed to identify the root causes of failure and assess the influence of weld-induced residual stresses.

The experimental results revealed that the weld heat-affected zone (HAZ), particularly at the curved head section of the vessel, exhibited reduced microhardness and structural integrity due to recrystallization and grain refinement. Hydrostatic testing confirmed that failure typically initiated in this thinned, weld-affected region, where residual tensile stresses were also found to be concentrated.

Numerical simulations further substantiated the experimental observations. Thermal-mechanical FEA demonstrated the presence of tensile residual stresses in the HAZ and identified stress concentrations aligned with experimentally observed crack zones. A two-stage FEA approach, incorporating both thermal and structural analyses, was used to simulate weld heat input and internal pressure loading. The resulting stress distributions and crack propagation patterns, evaluated using a semi-elliptical crack model, revealed that Mode I crack opening was dominant, especially at the head section.

Comparative analysis of critical stress intensity factors between the shell and head sections showed that the head region had a significantly lower threshold, explaining its susceptibility to catastrophic fracture. The numerical predictions showed strong correlation with experimental hydrostatic burst test results, validating the use of FEA in predicting failure mechanisms in deep-drawn welded vessels.

Overall, the study highlights the critical role of weld-induced residual stresses and geometric thinning in determining failure zones in pressure vessels. The integration of experimental and numerical techniques offers a robust framework for evaluating structural integrity and improving the safety of welded deep-drawn pressure vessels in industrial applications.

Keywords: MAG welding, welding heat input, finite element analysis, Gaussian heat flux approach.

Received April 17, 2025
Accepted August 22, 2025